

6. Propagation and Inundation Modeling

DEVELOPING QUANTITATIVE ESTIMATES for site-specific tsunami hazard assessments requires substantial modeling efforts to simulate potential tsunami impacts. For most locations, the use of historical data alone is not sufficient to derive long- and short-term hazard estimates. Such studies demand additional model data to fill in the gaps in the historical records. Even if a wealth of historical data is available, extra modeling estimates are warranted to account for changes of coastal infrastructure and/or for probable but non-historical events. The goals of numerical modeling for such studies differ substantially from the goals of a typical hindcast simulation, where the model results are compared with various field data for a specific historical event. In probabilistic modeling, comparison with historical data is only the first preliminary step of the study, to ensure reliability of multiple model estimates for probable events. In this respect, the probabilistic simulations are similar to forecast modeling, which employs a similar methodology for model use. This section presents the methods, modeling results, and discussions of the modeling study for Seaside, Oregon. This modeling effort produced a model database for probabilistic tsunami hazard assessment. Multiple simulations have been performed for a large number of potential far- and near-field tsunami sources using the MOST numerical model (Titov and González, 1997; Titov and Synolakis, 1996). Unlike previous tsunami probabilistic studies, high-resolution numerical grids are employed to resolve details and internal structure of the computed flood zones for each modeled event. Although Seaside does not have a tide gage to record historical tsunamis, some historical tsunami inundation data is available in the form of inundation zone estimates and tsunami sediment data for a limited number of historical events. The numerical model was tested against available historical tsunami measurements. Full numerical solutions for the high-resolution grid are retained for each model run to form a model database that can be used to perform various analyses and probabilistic estimates.

6.1 Numerical Model

NOAA's MOST numerical model (Titov and González, 1997; Titov and Synolakis, 1995, 1997) was utilized to produce inundation and propagation simulations for this study. This model has been extensively tested against a number of laboratory experiments and was successfully used for many historical tsunami simulations (Bourgeois *et al.*, 1999; Titov and Synolakis, 1995, 1996, 1997, 1998;

Yeh *et al.*, 1995). The model includes simulation of inundation dynamics by implementing moving boundary conditions that allow calculation of the flow dynamics of a wave climbing up dry topography and water withdrawing from the initial coastline. The employed numerical scheme also handles wave breaking that has been verified by comparison with a number of laboratory experiments and historical tsunami observations.

Details of the numerical implementation and testing of the MOST model are described in Titov and Synolakis (1995, 1996, 1997, 1998) and Titov and González (1997). Here, we present a brief description of the model and its application for this study.

6.1.1 Mathematical formulation

Two-dimensional shallow-water-wave equations (SW) are used to model this phenomenon. Despite certain limitations, these equations have proven capable of modeling many important physical characteristics of tsunami propagation, including wave breaking and bore runup on mild and steep beaches (Peregrine, 1966; Kobayashi *et al.*, 1987). Recent studies (Titov and Synolakis, 1995) have shown that this approximation works reasonably well even in the case of relatively short (length to depth ratio less than 10) breaking waves. Although the equations cannot resolve the specific pattern of the breaking front, they adequately model the overall wave behavior and give accurate estimations of the runup values in a wide range of wave parameters.

The shallow-water-wave equations are

$$\begin{aligned}h_t + (uh)_x + (vh)_y &= 0 \\u_t + uu_x + vu_y + gh_x &= gd_x \\v_t + uv_x + vv_y + gh_y &= gd_y\end{aligned}$$

where $h = \eta(x, y, t) + d(x, y, t)$, $\eta(x, y, t)$ is the wave amplitude, $d(x, y, t)$ is the undisturbed water depth, $u(x, y, t)$, $v(x, y, t)$ are the depth-averaged velocities in the x and y directions, respectively.

For arbitrary topography and bottom displacement the system of equations has to be solved numerically. We use a finite-differences algorithm based on the splitting method (Titov and Synolakis, 1998). This method reduces the numerical solution of the two-dimensional problem into the consecutive solution of two locally one-dimensional problems. The splitting technique allows effective implementation of a variety of boundary conditions, including moving boundary conditions, to account for tsunami inundation of dry topography.

Note that, with regards to wave breaking, the equations cannot resolve the specific pattern of the breaking front. However, the equations do adequately model the overall wave behavior and give accurate estimation of the runup values in a wide range of wave parameters. The MOST model handles wave breaking by modeling it as a shock wave within the shallow-water wave approximation (without simulating the details of the breaking front). The numerical dissipation qualities of the scheme allow for stable computation of the shock dynamics, conserving mass and momentum with good accuracy. The

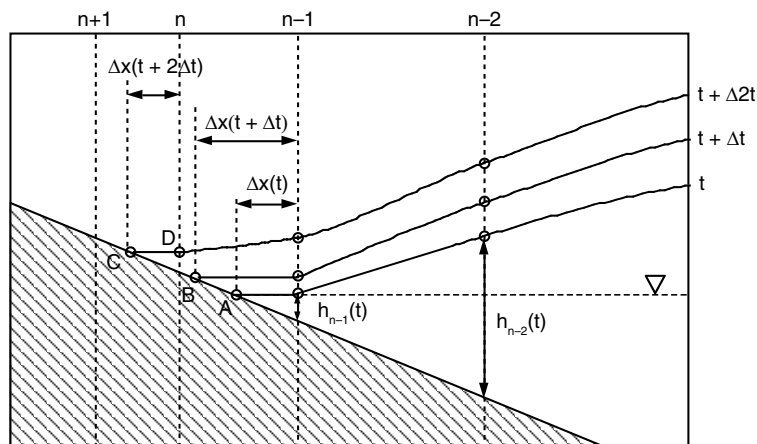


Figure 18: Definition sketch for the shoreline boundary computation.

amplitudes of the simulated breaking waves compare well with a number of laboratory experiments.

6.1.2 Moving boundary condition

To calculate tsunami evolution on a dry bed, it is necessary to use moving boundary conditions. The Froude number may be greater than 1 near the shoreline point, implying that all characteristic families have the same inclination in this region. Hence, it is impossible to use the direct relationships between the Riemann invariants, as is done for fixed boundary approximations (Titov and Synolakis, 1995). Therefore, approximations of the boundary values from previous space nodes are used. This is described in Fig. 18.

The shoreline algorithm uses a time-dependent space step $\Delta x(t)$ of the last node of the computational area. The objective is to maintain the shoreline boundary point (represented consecutively by A, B, or C on Fig. 18) on the surface of the beach during the computation. We therefore adjust the length of the last space step $\Delta x(t)$ every time step, so that the shoreline point (A) is at the intersection of the beach with the horizontal projection of the last “wet” point, for example, $n - 1$ node on Fig. 18. The value of the velocity on the shoreline node is equal to the velocity on the previous “wet” point.

We introduce additional grid points as follows. Referring to Fig. 18, at the time interval between times t and $t + \Delta t$, there are n grid points ($n - 1$ fixed grid points and the instantaneous shoreline, points A or B) in the computation. At time $t + 2\Delta t$, when the shoreline point (C) reaches beyond the next fixed grid point (n -th fixed node of the constant dry bed grid), this n -th fixed point is introduced between the shoreline point (C) and the previous internal fixed node ($n - 1$) and $\eta(D) = \eta(D)$. Now there are $n + 1$ grid points in the computational area and we repeat the process. During rundown, we reduce the number of dry grid points sequentially in an analogous manner.

6.1.3 Tsunami propagation model

To account for a spherical earth during tsunami propagation, the SW equations are solved in spherical coordinates. The MOST propagation code uses the non-linear shallow water equation in spherical coordinates with Coriolis force and a numerical dispersion scheme to take into account the different propagation wave speeds with different frequencies. The equations, shown below, are numerically solved using a splitting method (Titov and González, 1997):

$$h_t + \frac{(uh)_\lambda + (vh \cos \phi)}{R \cos \phi} = 0$$

$$u_t + \frac{uu_\lambda}{R \cos \phi} + \frac{vu_\phi}{R} + \frac{gh_\lambda}{R \cos \phi} - \frac{uv \tan \phi}{R} = \frac{gd_\lambda}{R \cos \phi} - \frac{C_f u \sqrt{u^2 + v^2}}{d} + fv$$

$$v_t + \frac{uv_\lambda}{R \cos \phi} + \frac{vv_\phi}{R} + \frac{gh_\phi}{R} + \frac{u^2 \tan \phi}{R} = \frac{gd_\phi}{R} - \frac{C_f v \sqrt{u^2 + v^2}}{d} - fu$$

where

- λ = longitude
- ϕ = latitude
- h = $\eta(\lambda, \phi, t) + d(\lambda, \phi, t)$
- $\eta(\lambda, \phi, t)$ = amplitude
- $d(\lambda, \phi, t)$ = undisturbed water depth
- $u(\lambda, \phi, t)$ = depth averaged velocity in longitude direction
- $v(\lambda, \phi, t)$ = depth averaged velocity in latitude direction
- g = gravity
- R = radius of the Earth
- f = $2\omega \sin \phi$, Coriolis parameter
- C_f = $gn^2/h^{1/3}$, n is Manning coefficient

To account for changing spatial scales during tsunami propagation, several telescoping grids are used for propagation simulations with dynamic data exchange at the boundaries. The highest resolution grid simulation includes inundation modeling with moving boundary conditions applied. The MOST model handles wave breaking by modeling it as a shock wave within the shallow-water wave approximation (without simulating the details of a breaking front). The numerical dissipation qualities of the scheme allow for stable computation of the shock dynamics, conserving mass and momentum with good accuracy. The amplitudes of the simulated breaking waves compare well with a number of laboratory experiments (Titov and Synolakis, 1995).

6.1.4 Model verification

MOST model testing against a variety of data is documented in many publications (see, for example, Bourgeois *et al.*, 1999; Titov and Synolakis, 1995, 1996, 1997, 1998; Yeh *et al.*, 1995).

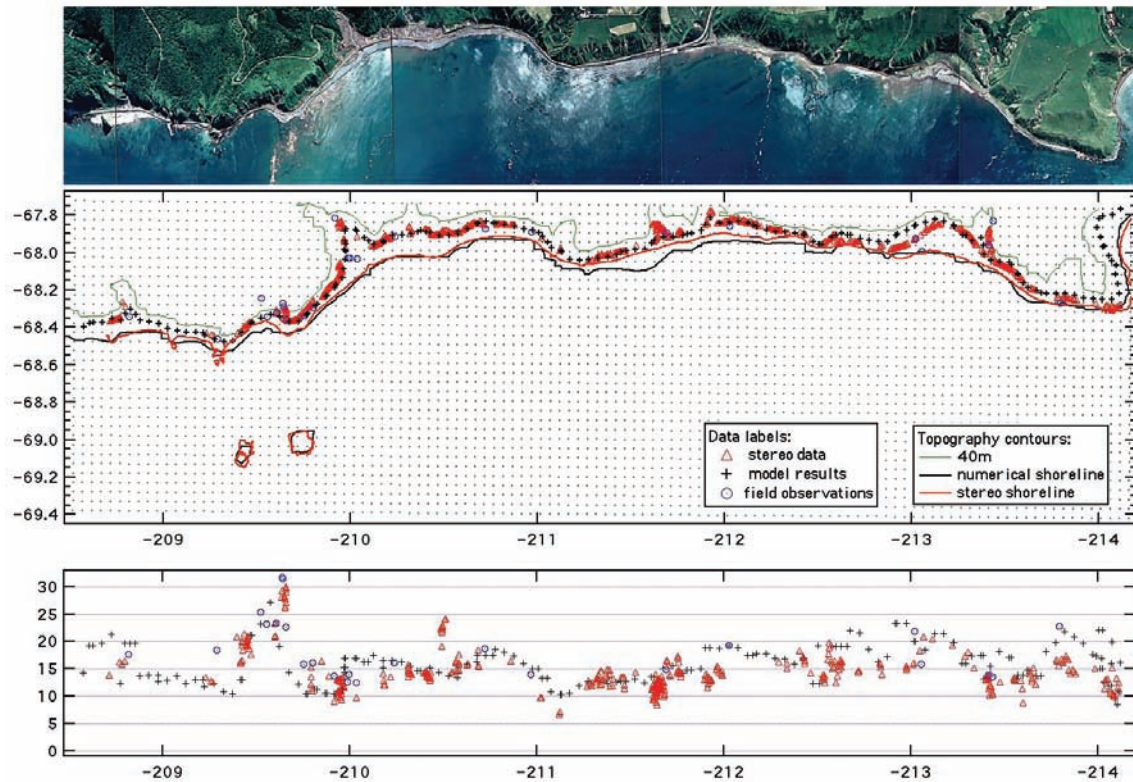


Figure 19: Comparison of the 1993 Okushiri tsunami inundation model (crosses) with field observations (circles) and stereo photo data (triangles). Top frame shows aerial photo of the modeled area used for the stereo analysis of the inundation data. Middle frame illustrates the numerical grid used for the simulation of the same area (dots are computational nodes, contours show topography data) and compares inundation distances. Bottom frame compares maximum vertical runup for the same shoreline locations.

Here, verification of the inundation computations is presented for one historical tsunami to illustrate the accuracy of inundation estimates using the MOST model. As a partial test of inundation forecast capability of the MOST model, the simulation of the 1993 Hokkaido-Nansei-Oki tsunami has been compared with an independent dataset. The model scenario of this event is based on the field survey data (Takahashi, 1996). An independent, much denser dataset of tsunami inundation distances and heights have been obtained at PMEL from stereo photography data of Okushiri Island. Figure 19 shows a comparison of the original MOST simulation (Titov and Synolakis, 1997) with the new stereo data. Inundation values are compared for the west coast of Okushiri Island, where the highest runup was measured for this event. The MOST runup and inundation estimates compare well with both stereo and field data.

6.2 Model Sources

Only earthquake-generated tsunamis are assumed for the Seaside probabilistic analysis. Landslide sources can potentially be considered for analyses in the

future, when the probability of landslide occurrence is better defined for this location.

Tsunamis propagated from distant sources have substantially different dynamics, duration, and intensity when compared with local tsunami events. Simulations of tsunami propagation across the Pacific from far-field sources need to be combined with the local high-resolution inundation computations. On the other hand, deformations from local earthquake sources change the bathymetry and topography of the study area, which needs to be taken into account during the simulation of inundation dynamics. To account for those and other differences, the modeling strategy for the tsunami scenarios of the far-field sources was different from the local sources' modeling.

6.2.1 *Far-field sources*

Seaside inundation modeling from far-field sources was divided into two steps: (1) across-ocean propagation from a source to the U.S. West Coast in the vicinity of Seaside and (2) high-resolution inundation simulation using the tsunami propagation results as input.

A source sensitivity study (Titov *et al.*, 1999) has established that only a few source parameters are critical for the far-field tsunami characteristics, namely the location and the magnitude (assuming some typical mechanism for the displacement and typical size of a given magnitude source). The details of the earthquake deformation are not important for inundation in the far-field. For example, wide-ranging variations of dip and slip (rake) angles of an earthquake source do not lead to significant changes in the far-field tsunami signal. Therefore, assuming simplified uniform slip for each location/magnitude combination of far-field sources accounts for most of the variability of the tsunami inundation at the Seaside (far-field) location for events of certain magnitude from a specified geographical area.

Tsunami propagation scenarios for far-field sources are obtained from PMEL's model tsunami propagation database that includes sources from all major tsunamigenic subduction zones (Titov *et al.*, 2005). The database contains a discrete set of unit sources that can provide the basis for constructing a tsunami scenario from a given source location and magnitude. Numerical solutions of tsunami propagation from these unit sources, when linearly combined, provide arbitrary tsunami propagation simulation. Figure 20 shows the computational area of the propagation simulations and locations of 14 earthquake scenarios considered for this study with earthquake magnitudes varying from M_w 8.2 to 9.2. Details of the earthquake parameters and the methodology for choosing the sources for the Probabilistic Tsunami Hazard Analysis are in Section 5, "Probabilistic Method."

6.2.2 *Near-field sources*

In contrast to tsunamis arriving from the far-field, details of the local earthquake deformation source are important for inundation estimates. The local source model for this study involved a discretized fault surface with variable

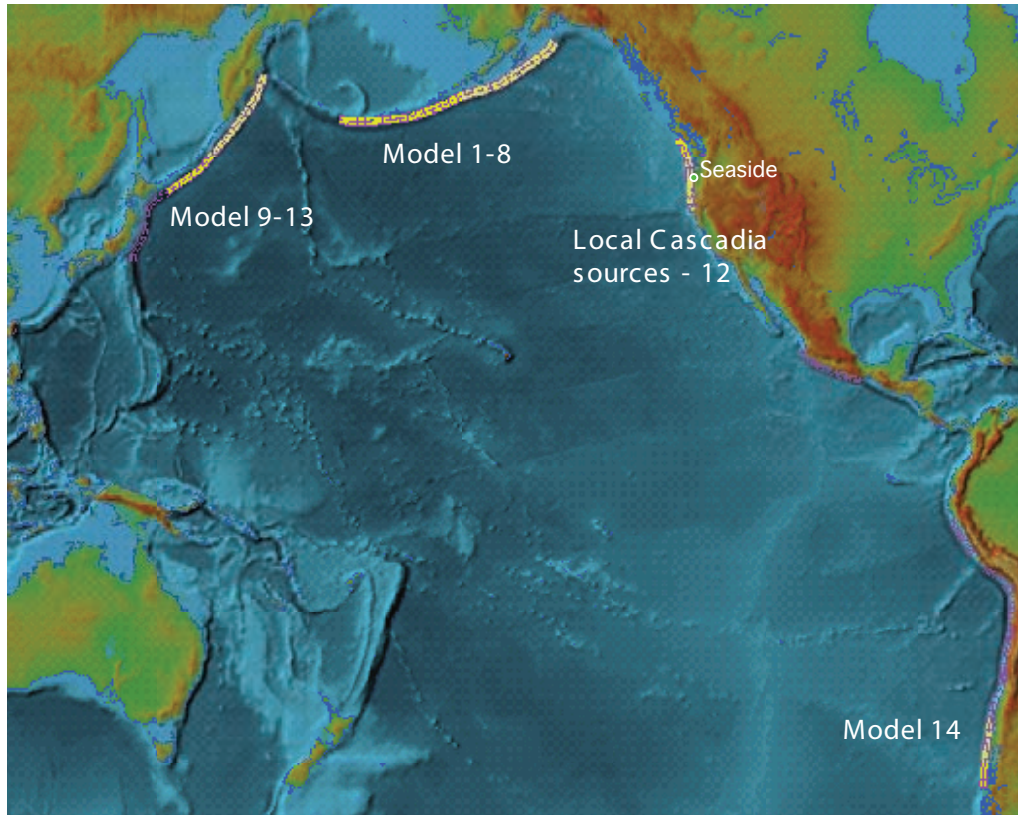


Figure 20: Source regions from FACTS database used for propagation modeling.

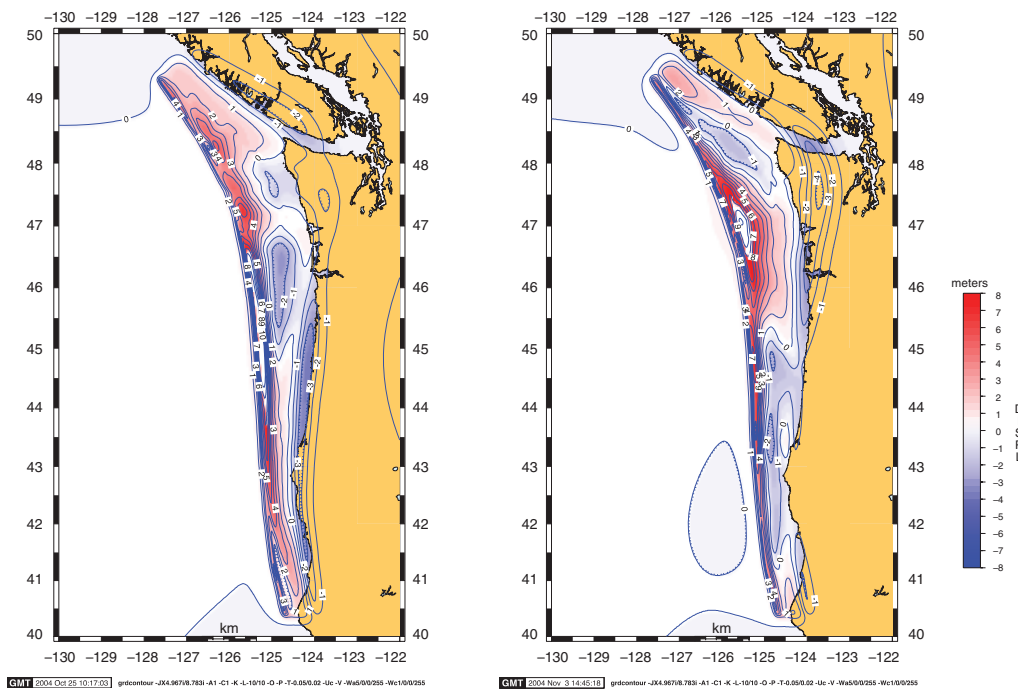


Figure 21: Two examples of coseismic vertical displacement field used as initial conditions for local tsunami modeling.

dip and strike, using average slip estimates, rupture dimensions, and moment magnitude estimates for the 1700 event. That allowed the use of different slip distribution patterns and different rupture geometries to estimate the range of local tsunamis. Figure 21 shows deformation patterns for two tsunami source scenarios of $M_w \sim 9$ earthquake used for the Seaside inundation modeling, as an example of source scenario variability. A total of 14 different local source scenarios were considered for the study.

6.3 Numerical Model Setup and Testing

Figure 22 illustrates the numerical grid system setup for the tsunami numerical model at Seaside. It shows the location and the resolution of three telescoping grids (grid A, B, and C with corresponding resolutions of 36, 6, and 1/3 arc seconds) that are used to compute each simulation of the Seaside tsunami inundation. The propagation results for the far-field sources (1964 propagation model is shown as an example on the Pacific-wide grid) are used as input through the boundary of grid A. The deformation data from local earthquake source scenarios are input directly into all three computational grids; the resulting local tsunamis are computed without additional use of the propagation model.

The MOST numerical model has been extensively tested in many model comparative studies and in various historical tsunami simulations (Titov *et al.*, 2005; Titov and González, 1997; Titov and Synolakis, 1995, 1998). It is known to accurately simulate tsunami propagation and inundation for even extreme tsunami events (Titov and Synolakis, 1995). The goal of the model tests in this study is to verify that the numerical setup for the Seaside, OR location is adequate for the purpose of this study, i.e., the accuracy, size, and the resolution of the numerical grid is sufficient to resolve details of the inundation flow for both the far-field and the near-field tsunamis.

Unfortunately, Seaside does not have a tide gage to record tsunami signals from the 1964 or other smaller tsunamis. It is not feasible to have a standard tide gage at Seaside because this would have to be located inside the very shallow entrance bar to the Necanicum River. To serve the needs of the northern Oregon coastal region, NOAA has installed a tsunami-capable tide gage at Garibaldi, a location that provides more direct observation of incident tsunamis.

Nonetheless, eyewitness reports of the 1964 Alaskan tsunami (compiled by Tom Horning and described in the Appendix C of this report) provide several tsunami runup values for this event at different Seaside locations. These are the best available tsunami field data for this location. The inundation measurements for this largest tsunami at Seaside are important, but they are not a comprehensive dataset to verify model accuracy. Changes in topography and bathymetry since 1964 create an additional difficulty in interpreting comparisons of the model simulations and field data.

The source of the 1964 Alaskan tsunami is modeled as a two-fault rupture with fault geometry and average slip values approximately corresponding to the analysis of Johnson *et al.* (1996). Detailed modeling of the 1964 event is beyond

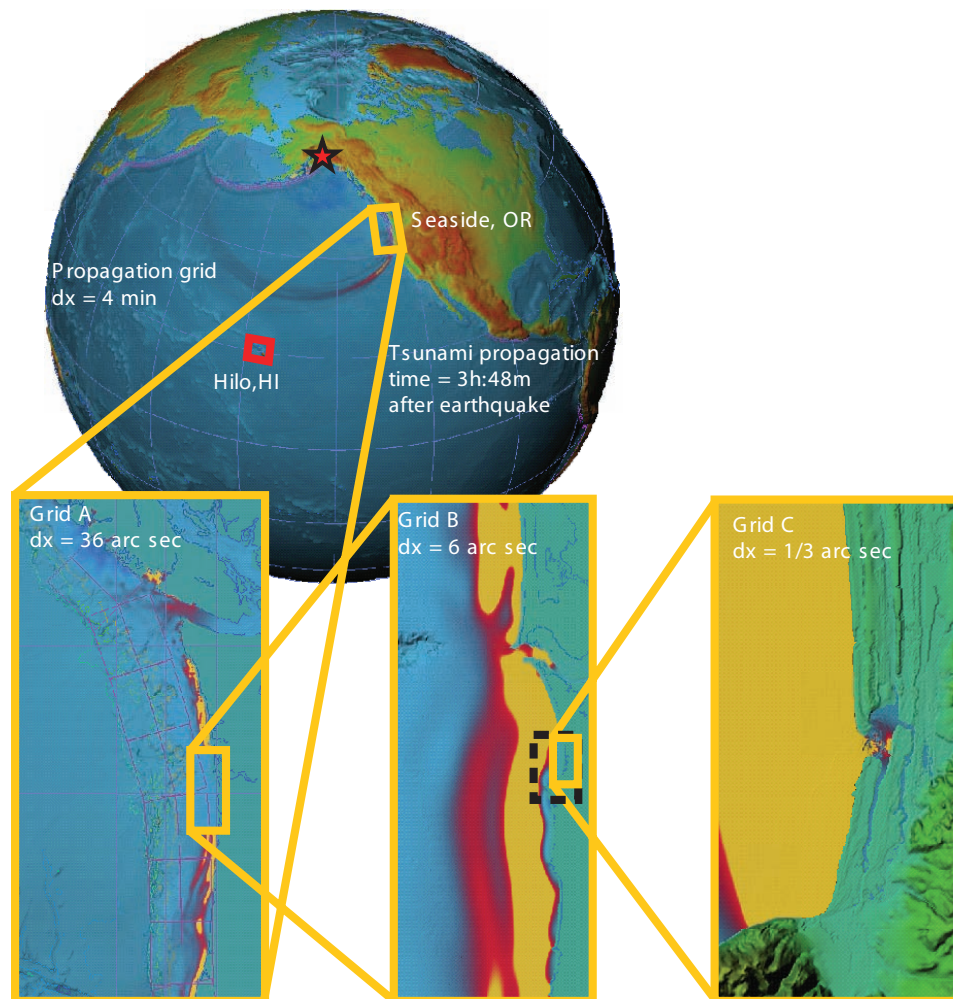


Figure 22: Schematic of nesting grids for Seaside, Oregon, used in numerical computations.

the scope of this study. The goal of this exercise is to accurately reproduce the far-field propagation pattern of this event. The sensitivity study (Titov *et al.*, 1999) implies that a simplified source model for this event that reflects the geometry, location, and magnitude of this source generates a tsunami that accurately reproduces the 1964 Prince William Sound tsunami in the far-field. To verify this assumption, we compared this model of the 1964 tsunami with a tide gage record at Hilo, Hawaii. To accurately reproduce the tsunami dynamics at Hilo, a high-resolution grid was used for the tsunami simulation. The overall model setup was similar to that used for the Seaside model, and consisted of three telescoping grids (Fig. 23) that used propagation model output as input via the outer grid boundary shown in red on Fig. 22. The numerical model setup for Hilo has been tested against many historical events and has been shown to be a reliable reference for verifying general parameters of the tsunami sources. The results shown in Fig. 23 demonstrate that our propagation model of the 1964 tsunami compares well with the tide gage record. The amplitude

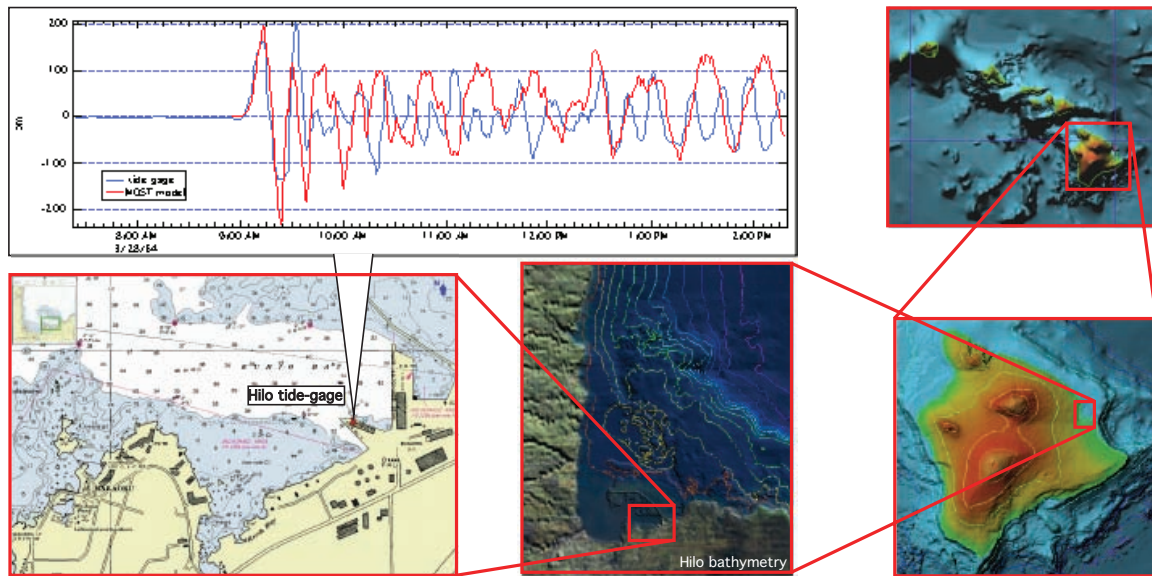


Figure 23: Schematic of nesting grids for Hilo, Hawaii, where the modeled 1964 tsunami is compared with tide gauge records.

and period of the first two waves match with the measured data. The first waves carry most of the information about the tsunami source magnitude and configuration. Therefore, the comparison at Hilo shows that our model source of the 1964 tsunami has proper amplitude and correct location. These are the two most important parameters of the source for reproducing the tsunami amplitude in the far-field (Titov *et al.*, 1999). The good comparison with independent data at Hilo provides additional confirmation of the accurate representation of the 1964 tsunami at Seaside.

The comparison of modeled inundation of the 1964 tsunami at Seaside with the eyewitness accounts shows a qualitatively consistent picture. Figure 24 shows the computed inundation and the inundation inferred from the eyewitness accounts. The computed inundation shows a slightly larger inundated area; however, comparisons of the vertical runup values at the open coast show very good correspondence between measurements and model. The difference between the model inundation extent and the field estimates can be explained by many factors, including slight differences of coastal dune representation in the Digital Elevation Model used for this study and the actual topography in 1964. The most important value for this study is the predicted vertical amplitude values. The predicted runup for the 1964 tsunami compares well with measurements, which ensures the accuracy of the tsunami inundation model predictions. The Seaside inundation model of the 1964 tsunami was computed with two different grid resolutions of 30 m and 10 m. The comparison of the results shows that computed vertical runup values are very similar for both simulations, while the horizontal extent of the inundation differs. The 30-m grid does not represent the coastal dunes accurately enough, which leads to extended inundation areas for waves that have smaller amplitudes than the height of the dunes. Therefore, the 10-m grid was used for all far-field simulations, in which case the coastal dunes can block the horizontal extent

of smaller amplitude waves. For the local tsunami sources, where the runup values are much larger, small-scale features like dunes do not make much difference in the horizontal inundation. The 30-m grid with coverage of a larger area was used to account for much greater inundation distances.

Data for the 1700 Cascadia tsunami are much scarcer. Tsunami deposit data are the only indication of the size of the tsunami inundation area. Since topography and bathymetry could have changed significantly in 300 years, a direct comparison with the model data is very difficult. Our inundation results for the local tsunami sources (which are all potential scenarios for the 1700 event) show that computed inundation areas encompass the tsunami sediment locations. At least qualitatively, this indicates that our local inundation estimates are within the constraints of the available field data for such events.

6.4 Database of Model Runs

Computed tsunami inundation scenarios for Seaside are stored in a WWW-accessible database for further analyses. All computed variables (amplitude and velocity components) are saved at each time-step for the duration of the simulation.

These model data are available via Web interface using Live Access Server (LAS) technology (Fig. 25). The interface provides full access to all computed variables and additional tools for project researchers to conduct additional analyses.

6.4.1 Discussion of model simulation results

Analysis of the far-field tsunami source simulations revealed the strong influence of the directivity of tsunami propagation on runup amplitudes at Seaside. Directivity determines both the amplitude and the direction of the incident waves and, therefore, affects the degree of refraction and other effects of local and regional bathymetry and shoreline shape have on the characteristics of tsunamis at Seaside. Potentially important local and regional features include the Astoria Canyon, the bight between the Columbia River and Tillamook Head just south of Seaside, the Juan de Fuca Ridge, and seamount chains farther offshore. These bathymetric features are resolved in the DEM used to model tsunami propagation to Seaside. A detailed analysis of these effects has not been carried out. However, such an analysis would be helpful for interpreting the tsunami response in the Seaside area as a function of the source location.

Figure 26 illustrates the overall effects of different sources by comparing three different simulation results corresponding to Source Numbers 2, 3, and 5 in Table 6. The figure shows that these three simulation scenarios are for tsunami sources at similar locations (epicenters for these three earthquakes could very well be at the same location); all correspond to the same earthquake magnitude of $M_w = 9.2$. Despite the seeming similarities of these source scenarios, the inundation simulations at Seaside show very different amplitudes (lower images). The difference is explained by different propagation directivity patterns for the three sources (upper images). The largest inundation at Sea-

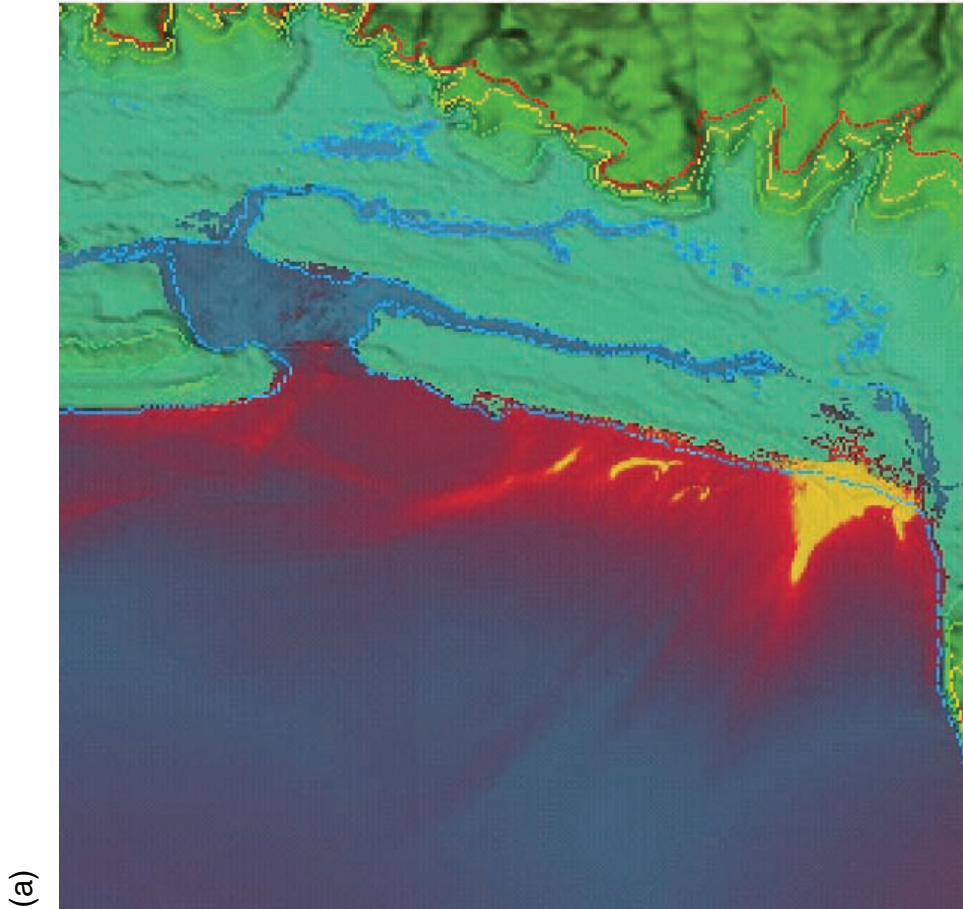
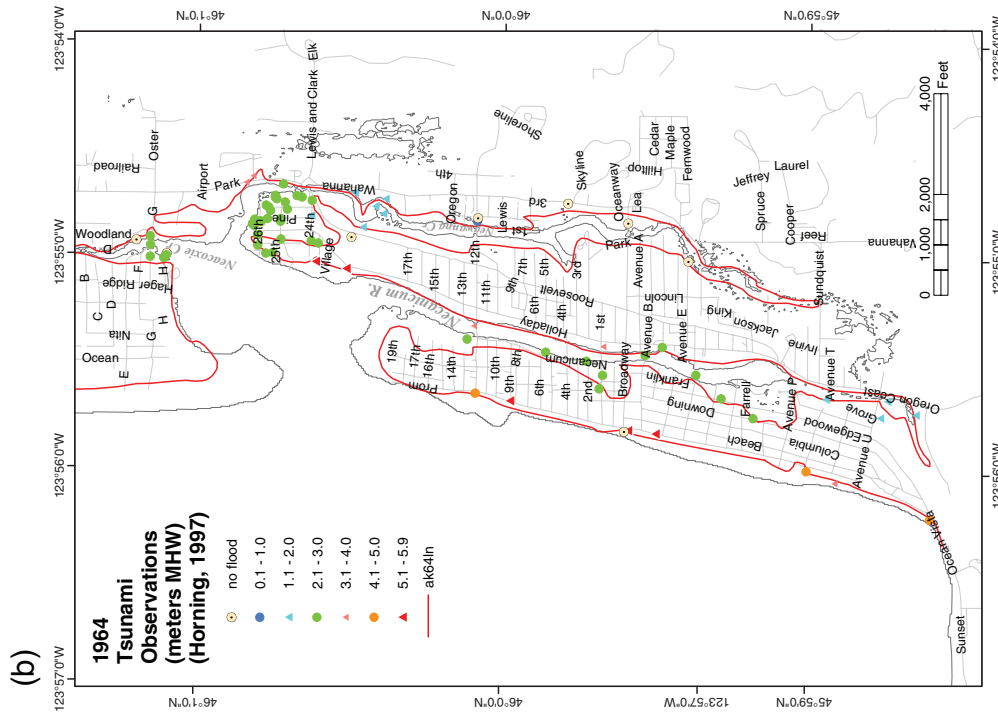


Figure 24: (a) Predicted peak tsunami amplitudes from far-field sources at Seaside, Oregon, compared with (b) eyewitness observations for the 1964 tsunami.

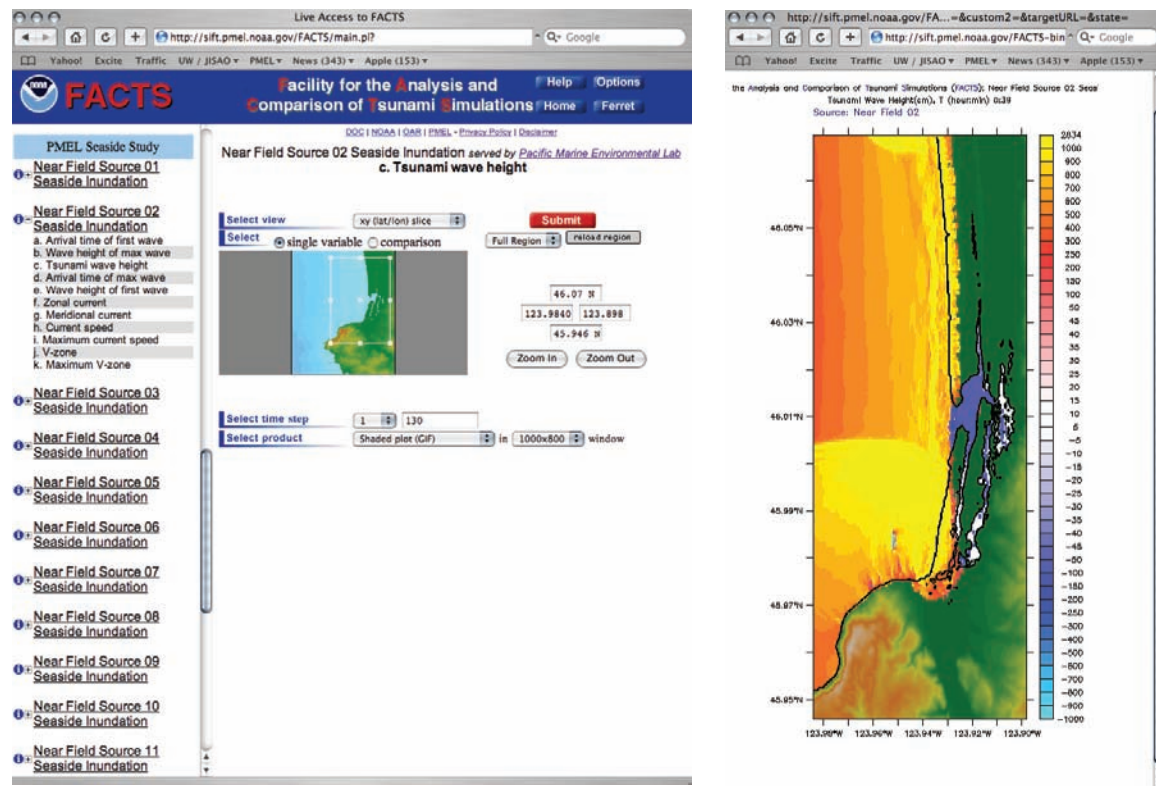


Figure 25: Screen-shot from FACTS database.

side among the chosen far-field sources is produced by the Alaskan source with the fault near Kodiak (the middle images). This source roughly corresponds to the rupture area of the 1964 Prince Williams Sound tsunami but have different slip distribution. This large inundation from the far-field source may not show up in the probabilistic inundation map for Seaside due to the lower probability of such a source. However, it should be noted that tsunami sources from this area in Alaska could produce large inundation at Seaside if this low-probability rupture does occur.

Currents cannot be neglected in tsunami hazard assessments, because the associated kinetic energy can be the most destructive aspect of a tsunami and very high currents can be associated with relatively modest wave height. Figure 27 illustrates this point for the far-field Source Numbers 3 and 5 of Table 6. Note that regions of high currents frequently do not correspond to regions of high wave heights. The most obvious examples are in the river entrance and the adjacent bay area for both scenarios and, especially in the case of Source Number 3, on the peninsula south of the river entrance. This lack of correspondence between maximum wave heights and currents means that inundation maps of maximum wave height could be dangerously misleading—i.e., the overall tsunami hazard and destructive potential could be seriously underestimated in areas of modest wave height because destructively high currents were not taken into account. A more complete hazard assessment must employ “impact indices” or “impact metrics” that take account of both

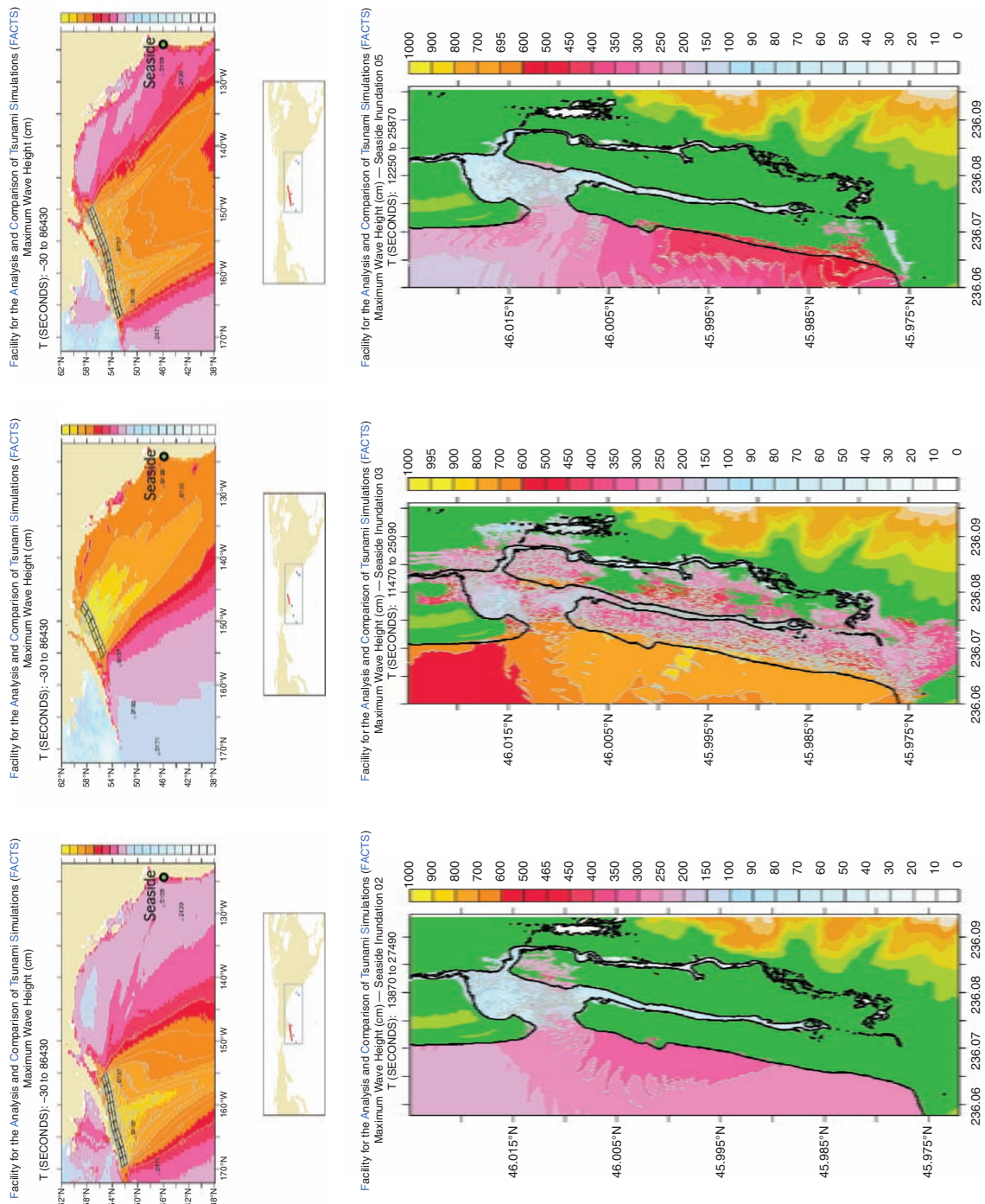


Figure 26: Example of how tsunamis beaming from different earthquakes along the Aleutian-Alaska Subduction Zone affect tsunami amplitudes at Seaside.

potential and kinetic energy, i.e., both wave height and currents. This topic is explored in Section 7, “Evaluating Tsunami Impact Metrics.”

For local sources, in Fig. 28 we compare the inundation map derived from one of the slip distributions used for Cascadia Subduction Zone earthquakes described above to the inundation map derived from a uniform slip rupture model described by Priest *et al.* (1997) (their Model 1A). Although the magnitudes for these two scenarios is similar and the average slip used in Fig. 28a is similar to the uniform slip used for Fig. 28b, the distributed slip model results in significantly higher maximum wave heights. This is consistent with theoretical results (Geist and Dmowska, 1999) and the comparison presented in Priest *et al.* (1997) between the uniform slip model and the same model with an added Gaussian asperity (Model 1A-Asperity). The difference between the inundation maps derived from uniform slip and distributed slip source models is shown in Fig. 28c.

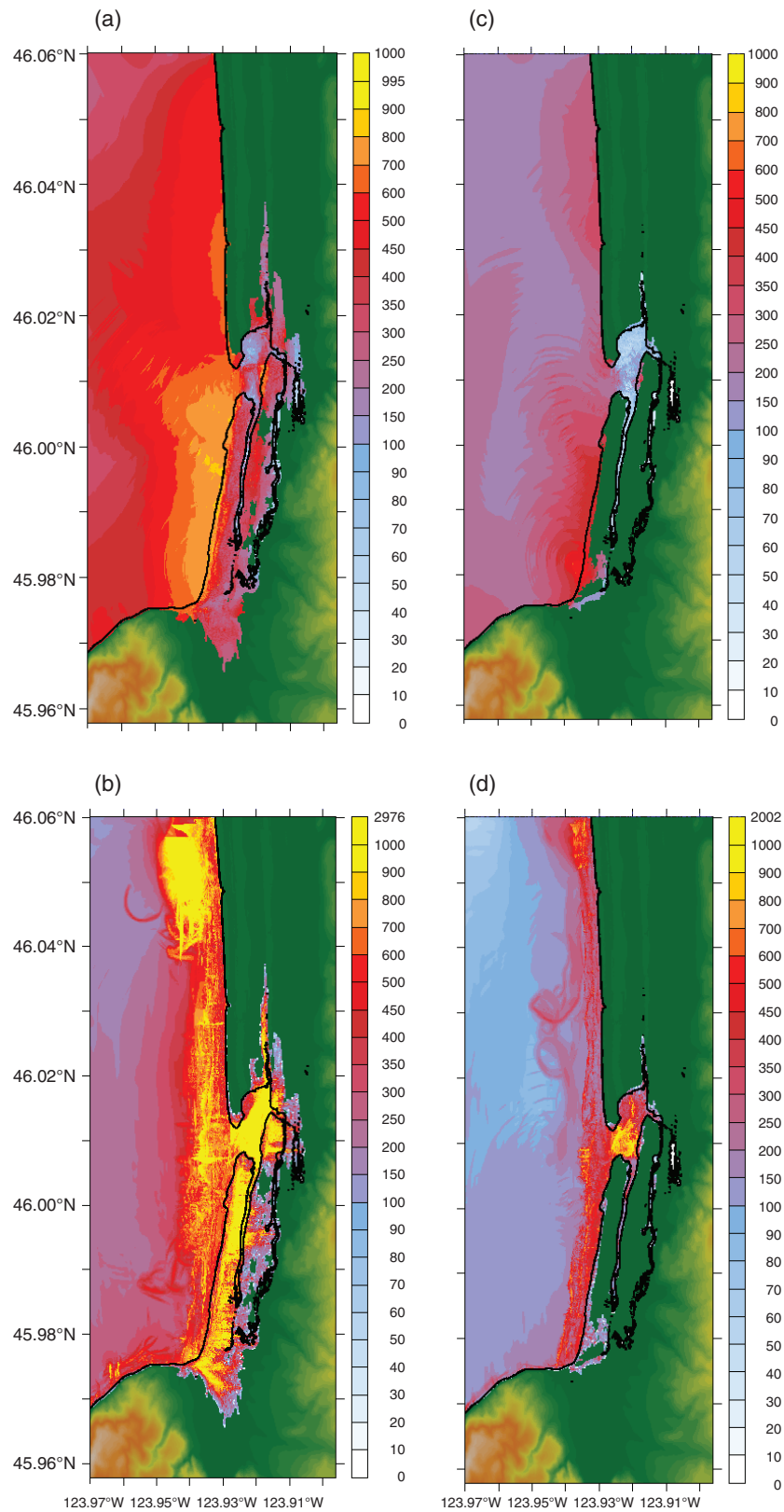


Figure 27: Maximum wave heights and currents for Sources 3 and 5 in Table 6. (a) Source 3 maximum wave height, (b) Source 3 maximum current speed, (c) Source 5 maximum wave height, (d) Source 5 maximum current speed.

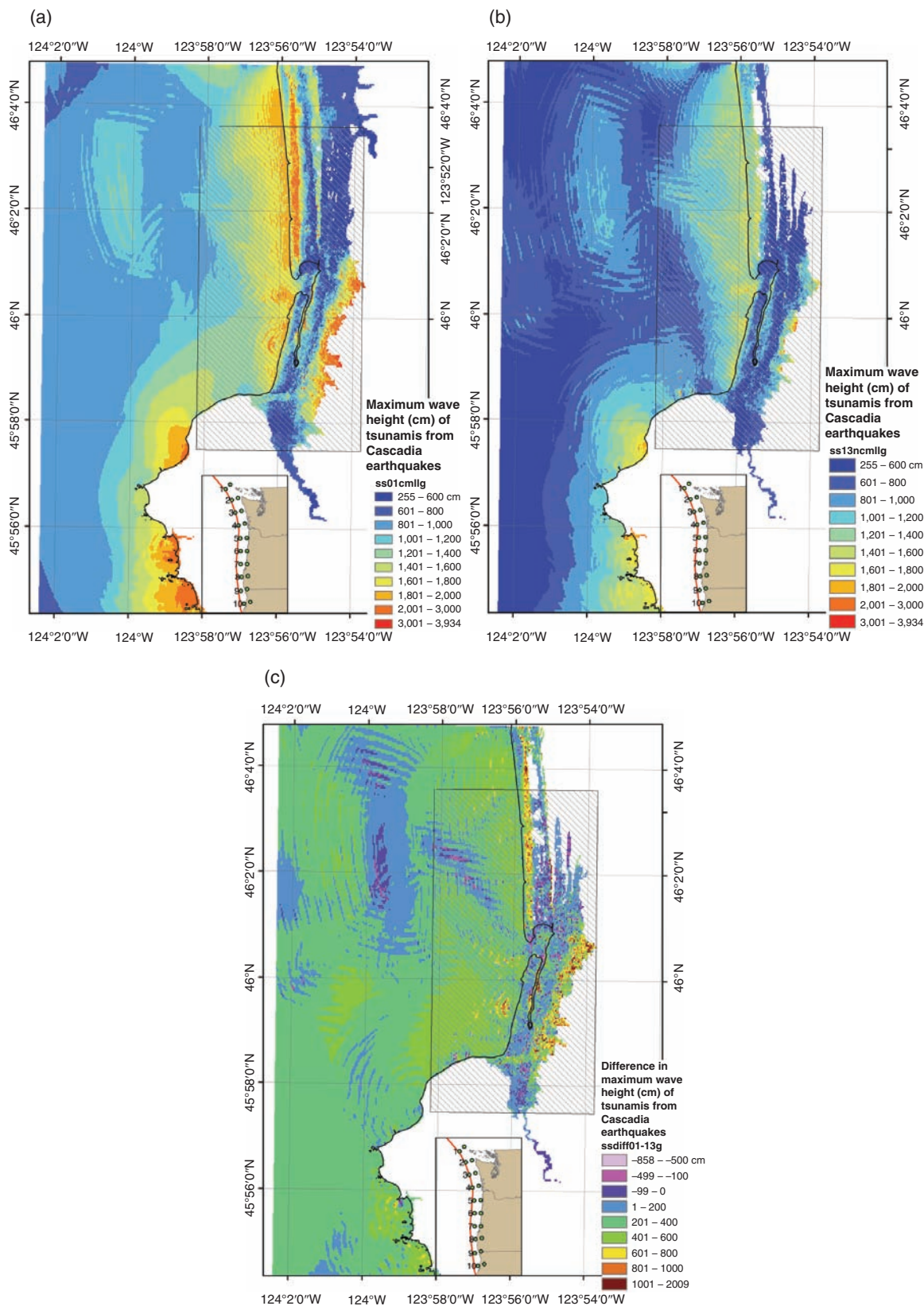


Figure 28: Comparison of inundation maps using (a) the distributed slip source described in this study with (b) the uniform slip source (Model 1A) described by Priest *et al.* (1997). Map (c) is the difference of wave heights between (a) and (b).